



Contents lists available at ScienceDirect

Catalysis Today

journal homepage: www.elsevier.com/locate/cattod



HDS performance of NiMo catalysts supported on nanostructured materials containing titania

Julio Cesar Morales-Ortuño^a, Rodrigo Arturo Ortega-Domínguez^a,
Patricia Hernández-Hipólito^a, Xim Bokhimi^b, Tatiana E. Klimova^{a,*}

^a Laboratorio de Nanocatálisis, Departamento de Ingeniería Química, Facultad de Química, Universidad Nacional Autónoma de México (UNAM), Cd. Universitaria, Coyoacán, 04510, México D.F., Mexico

^b Instituto de Física, Universidad Nacional Autónoma de México (UNAM), Apartado Postal 20-364, 01000, México D.F., Mexico

ARTICLE INFO

Article history:

Received 13 April 2015

Received in revised form 25 July 2015

Accepted 27 July 2015

Available online xxx

Keywords:

Deep hydrodesulfurization

NiMo catalysts

Titania nanotubes

Ti-SBA-15

Ti-SBA-16

Support effect

ABSTRACT

In the present work, NiMo catalysts supported on titania-containing materials of the SBA family (Ti-SBA-15 and Ti-SBA-16) and on titania nanotubes of different pore diameters were prepared with the aim of selecting the most promising catalysts for deep hydrodesulfurization (HDS) of gas oil. Supports and catalysts were characterized by nitrogen physisorption, XRD, temperature programmed reduction, ammonia TPD, UV–vis DRS and scanning electron microscopy (SEM-EDX). Sulfided catalysts were characterized by HRTEM and tested in the simultaneous HDS of dibenzothiophene (DBT) and 4,6-dimethyldibenzothiophene (4,6-DMDBT). For comparison purposes, a conventional NiMo/ γ -Al₂O₃ catalyst was used. In HDS of DBT, all catalysts supported on titania-containing nanostructured materials showed similar activity as the NiMo/ γ -Al₂O₃ reference, but in HDS of 4,6-DMDBT their activities were about twice higher than that of NiMo/ γ -Al₂O₃. Regarding selectivity, for DBT HDS, the presence of titania in the supports resulted in an increase in the proportion of CHB product, whereas for 4,6-DMDBT different behavior was observed. Thus, NiMo catalysts supported on Ti-SBA-15 and Ti-SBA-16 showed similar selectivity as the NiMo/ γ -Al₂O₃. On the contrary, the catalysts supported on titania nanotubes allowed reaching high conversions of 4,6-DMDBT with a much lower proportion of hydrogenated products, which is an interesting result not observed by us previously.

© 2015 Elsevier B.V. All rights reserved.

1. Introduction

In the last decade, it has become necessary to increase significantly the production of clean fossil fuels and at the same time, to improve their quality in order to comply with new environmental legislations worldwide. Decreasing the sulfur and nitrogen content in petroleum derived fuels should improve air quality by diminishing CO, CO₂, NO_x and SO_x emissions in urban zones. In general, hydrotreatment (HDT) processes are employed in the oil-refining industry to remove heteroatoms (S, O and N), metals and aromatics. Therefore, the development of novel more active and effective HDT catalysts is currently an important task. Among HDT processes, hydrodesulfurization (HDS) is commonly used to eliminate sulfur from different petroleum fractions [1]. The HDS process is commonly performed at high temperature and pressure, in a hydrogen atmosphere and in the presence of a heterogeneous cat-

alyst. Traditionally, bimetallic catalysts based on Mo/W, promoted by Ni/Co and supported on γ -Al₂O₃ are used in the HDS process. These catalysts exhibit high activity in removing sulfur from non-refractory thiophene, benzothiophene and dibenzothiophene compounds, but their activity is relatively low in removing sulfur from refractory dibenzothiophenes with alkyl groups in positions 4 and 6 of the molecule (positions close to the sulfur atom) [2,3]. This leads to the production of diesel fuel, which after conventional hydrotreatment still contains a noticeable amount of unreacted refractory dibenzothiophene compounds (about 500–1000 ppm of S). Nowadays, the challenge is the development of a new generation of catalysts highly active for the removal of low reactive dibenzothiophenes, which is the key for obtaining ultra-low sulfur diesel (ULSD) containing less than 15 ppm of S [4]. Recently, a new generation of commercial bulk hydroprocessing catalysts has been developed for the production of ULSD, such as NEBULA (New Bulk Activity) and STARS (Super Type II Active Reaction Sites) catalysts [5–7]. These catalysts have high activity in HDS [8], but they are expensive because of their high metal content and high consumption of hydrogen [9–12]. From this point of view, supported HDS

* Corresponding author.

E-mail addresses: klimova@unam.mx, tklimova@gmail.com (T.E. Klimova).

catalysts with low metal content and better textural characteristics can be an attractive option for the substitution of expensive bulk HDS catalysts in industry.

It is well-known that the catalytic performance of HDS catalysts can be modified by changing the nature of the active phase or of the support. Among many different materials tested as supports for HDS catalysts, titania has attracted special attention due to high intrinsic HDS activity demonstrated by Mo catalysts supported on this oxide [13,14]. This behavior of TiO₂-supported Mo catalysts was attributed to the good dispersion of Mo oxide species and their easy reduction and sulfidation. In order to take advantage of the attractive properties of titania and increase its specific surface area, different combinations of TiO₂ with other oxide supports or TiO₂-containing mixed oxides were assayed as supports giving promising results. Among many different titania-containing supports, new nanostructured materials have attracted special attention in the last decade. This is due to their unique physical and chemical properties, novel morphology and attractive texture. Thus, in our group, the well-ordered mesoporous molecular sieves SBA-15 and SBA-16 modified with titania were synthesized and tested as supports for NiMo catalysts, giving good results, especially for the elimination of low reactive aromatic sulfur compounds, such as alkyl-substituted dibenzothiophenes [15,16]. In addition, novel titania-based nanoscale materials (nanocrystals, nanoparticles, nanotubes, nanowires and nanofibers) have appeared recently. Some of them have already been tested as supports for HDS catalysts. For example, CoMo catalysts supported on high surface area (more than 300 m²/g) nano-structured titania powder showed activity twice higher in dibenzothiophene HDS than a commercial CoMo/alumina catalyst [17]. CoMo catalysts supported on titania nanotubes also showed high activity in HDS of dibenzothiophene [18,19] and selective hydrodesulfurization of thiophene [20]. High HDS activity observed in the above works was attributed to high dispersion of catalytically active MoS₂ particles and high sulfidability of Mo species [17–19]. Regarding NiW catalysts, it was also found that the catalysts supported on TiO₂ nanotubes resulted in two times higher thiophene conversion in comparison with the alumina and titania supported ones [21]. The above results show that nanotubular titania is a promising support for hydrotreating catalysts. However, up to now, the catalytic behavior of the HDS catalysts supported on titania nanotubes has not been studied in the elimination of sulfur from refractory alkyl-substituted dibenzothiophenes.

In the present work, our interest was to inquire into the catalytic behavior of the NiMo catalysts supported on titania nanotubes in deep hydrodesulfurization (HDS) and to compare their activity and selectivity with those of Ti-SBA-15 and Ti-SBA-16 supported analogs. For this purpose, NiMo catalysts supported on titania-containing materials of the SBA family (Ti-SBA-15 and Ti-SBA-16) and on titania nanotubes of different pore diameters were prepared and characterized. Their catalytic activity was tested in simultaneous HDS of two model compounds: dibenzothiophene (DBT) and 4,6-dimethyldibenzothiophene (4,6-DMDBT). These compounds were selected as representative molecules of the gas oil fraction, which have different reactivity toward the direct desulfurization and hydrogenation routes of HDS.

2. Experimental

2.1. Support and catalyst preparation

Gamma alumina support (γ -Al₂O₃) was synthesized by calcination of Boehmite Catapal B at 700 °C for 4 h. Mesoporous SBA-15 silica support with hexagonal *p6mm* structure was prepared according to a well-known procedure [22,23] using the triblock copolymer Pluronic P123 (M_{av} = 5800, EO₂₀PO₇₀EO₂₀, Aldrich) as

the structure-directing agent and tetraethyl orthosilicate (TEOS, Aldrich, 99.999%) as the silica source. Pluronic P123 (4 g) was dissolved in water (30 g) and 2 M HCl (120 g) solution at 35 °C. Then TEOS (8.5 g) was added into the solution. The mixture was stirred at 35 °C for 20 h and then aged at 80 °C for 48 h without stirring. The solid product was recovered by filtration, washed with deionized water and air-dried at room temperature. Calcination was carried out in static air at 550 °C for 6 h. SBA-16 silica with cubic *Im $\bar{3}m$* structure was synthesized according to the literature [24,25] using the triblock copolymer Pluronic F127 (EO₁₀₆PO₇₀EO₁₀₆, BASF) as the structure-directing agent and tetraethyl orthosilicate as the silica source. The same amounts of reactants were used as for the synthesis of the SBA-15 material. The mixture was stirred at 35 °C for 20 h and then aged at 100 °C for 72 h without stirring. The solid product was recovered by filtration, washed, dried and calcined as described for SBA-15. Synthesized SBA-15 and SBA-16 materials were modified with titania by chemical grafting using titanium(IV) isopropoxide (Ti(i-PrO)₄, Aldrich, 97%) as the titania source and dry ethanol as the solvent. In the grafting procedure, calcined SBA-15 or SBA-16 material was slurried in ethanol solution containing Ti(i-PrO)₄ for 6 h. To eliminate the excess Ti(i-PrO)₄, the filtered material was washed three times with dry ethanol. After drying at room temperature Ti-SBA-15 and Ti-SBA-16 materials were calcined in static air at 550 °C for 5 h. Elemental analysis of titania-containing SBA-15 and SBA-16 materials (SEM-EDS) showed that they contained 16 and 14 wt.% of TiO₂, respectively. Titania nanotubes (NT) were synthesized by alkaline hydrothermal treatment (10 M NaOH, 140 °C, 20 h) of commercial TiO₂ followed by ion exchange with 0.1 M HCl solution and drying (120 °C, 12 h) [26,27]. Two NT supports were synthesized using two different anatase precursors: low surface area TiO₂ (7.6 m²/g, Aldrich) and anatase nanopowder (89 m²/g, Aldrich). Nanotubular materials with internal pore diameter of 3 nm and 5 nm, respectively, were obtained. These supports were labeled as NT(3) and NT(5).

NiMo catalysts supported on Ti-SBA-15, Ti-SBA-16, NT(3), NT(5) and γ -Al₂O₃ were prepared by incipient wetness co-impregnation of aqueous solutions of nickel nitrate, Ni(NO₃)₂·6H₂O (Aldrich), and ammonium heptamolybdate, (NH₄)₆Mo₇O₂₄·4H₂O (Merck). After co-impregnation, all catalysts were dried first at room temperature, then at 100 °C for 24 h, and calcined at 500 °C for 4 h (Ti-SBA and alumina-supported samples) and at 350 °C for 2 h (NT-supported catalysts) in air atmosphere. The nominal composition of the catalysts was 12 wt.% of MoO₃ (8×10^{-4} mol/g) and 3 wt.% of NiO (4×10^{-4} mol/g), which corresponds to the Ni:Mo molar ratio = 1:2. Prepared catalysts will be denoted as NiMo/corresponding support.

2.2. Support and catalyst characterization

Supports and prepared NiMo catalysts were characterized by N₂ physisorption, X-ray diffraction (XRD), UV–vis diffuse reflectance spectroscopy (DRS), NH₃ temperature-programmed desorption (TPD), temperature-programmed reduction (TPR), scanning electron microscopy (SEM-EDX) and high-resolution transmission electron microscopy (HRTEM). N₂ adsorption/desorption isotherms were measured with a Micromeritics ASAP 2020 automatic analyzer at liquid N₂ temperature. Prior to the experiments, the samples were degassed ($p < 10^{-1}$ Pa) at 270 °C for 6 h. Specific surface areas were calculated by the BET method (S_{BET}), the total pore volume (V_p) was determined by nitrogen adsorption at a relative pressure of 0.98 and pore size distributions were obtained from the adsorption isotherms by the BJH method. The mesopore diameter (D_p) corresponds to the maximum of the pore size distribution. The micropore area (S_{μ}) was estimated using the correlation of t-Harkins & Jura (*t*-plot method). XRD patterns were recorded in the $3^\circ \leq 2\theta \leq 90^\circ$ range on a Siemens D5000 diffractometer,

using $\text{CuK}\alpha$ radiation ($\lambda = 1.5406 \text{ \AA}$) and a goniometer speed of $1^\circ(2\theta) \text{ min}^{-1}$. Small-angle XRD ($2\theta = 0.5\text{--}10^\circ$) was performed on a Bruker D8 Advance diffractometer using small divergence and scattering slits of 0.05° . UV–vis electronic spectra of the samples were recorded in the wavelength range 200–800 nm using a Varian Cary 100 Conc spectrophotometer equipped with a diffuse reflectance attachment. Polytetrafluoroethylene was used as reference. NH_3 TPD and TPR experiments were carried out in a Micromeritics AutoChem II 2920 automatic analyzer equipped with a TC detector. Before ammonia adsorption, the samples were pretreated in situ at 500°C for 30 min in a helium flow in order to remove water and other contaminants. The samples were then cooled to 120°C and contacted with a He/NH_3 mixture (90/10 mol/mol and 20 mL/min) for 30 min. The desorption step was performed in a He stream (50 mL/min) with a heating rate of $10^\circ\text{C}/\text{min}$. After reaching 500°C , the sample was kept at this temperature until the trace reached the base line. Before TPR experiments, the samples were pretreated in situ at 500°C for 2 h under air flow and cooled in an Ar stream. The reduction step was performed under a stream of an Ar/H_2 mixture (90/10 mol/mol and 50 mL/min), with a heating rate of $10^\circ\text{C}/\text{min}$ up to 1000°C . Chemical composition of the synthesized materials was determined by SEM-EDX using a JEOL 5900 LV microscope with OXFORD ISIS equipment. HRTEM studies were performed using a JEOL 2010 microscope (resolving power 1.9 Å). The solids were ultrasonically dispersed in heptane and the suspension was collected on carbon-coated grids. Slab length and layer stacking distributions of MoS_2 crystallites in each sample were established from the measurement of at least 300 crystallites detected on several HRTEM pictures taken from different parts of the same sample dispersed on the microscope grid.

2.3. Catalytic activity tests

The HDS activity tests were performed in a batch reactor at 300°C and 7.3 MPa total pressure for 8 h using *n*-hexadecane solution of DBT (1300 ppm of S) and 4,6-DMDBT (500 ppm of S). Prior to the catalytic activity evaluation, the catalysts were sulfided ex situ in a tubular reactor at 400°C for 4 h in a stream of 15 vol.% of H_2S in H_2 under atmospheric pressure. The sulfided catalysts (0.15 g) were transferred in an inert atmosphere (Ar) to a batch reactor (Parr) with 40 mL of *n*-hexadecane solution containing the model compounds (DBT and 4,6-DMDBT). The course of the reaction was followed by withdrawing aliquots each hour and analyzing them on an Agilent 6890 gas chromatograph. To corroborate product identification, the product mixture was analyzed on an Agilent 7890A GC system with 5975C MS detector.

Kinetic studies were performed in the absence of the external and internal mass transfer/diffusion limitations. Catalyst activity was determined by measuring DBT and 4,6-DMDBT concentrations at different reaction times. DBT and 4,6-DMDBT conversions (X) were calculated as:

$$X = \frac{C_0 - C}{C_0} \quad (1)$$

where C_0 is the initial DBT (or 4,6-DMDBT) concentration (mol L^{-1}) in the reaction mixture and C is its concentration (mol L^{-1}) at different reaction times (t , h). The rate constants (k_{DBT} and k_{DMDBT} , Tables 6 and 7) were determined considering that the DBT and 4,6-DMDBT HDS reactions are of the pseudo-first-order using the following equation:

$$k = -\frac{1}{t} \times \ln(1 - X) \quad (2)$$

where k is the pseudo-first-order reaction constant (h^{-1}), X the DBT (or 4,6-DMDBT) conversion and t the reaction time (h). Linear plots

used for k_{DBT} and k_{DMDBT} calculations are shown in Fig. 11. Obtained k (h^{-1}) values were also expressed in $\text{L s}^{-1} \text{ g}_{\text{cat}}^{-1}$ (Tables 6 and 7) in order to obtain values comparable with those published previously.

3. Results and discussion

3.1. Supports

Fig. 1 shows TEM micrographs of the supports synthesized in the present work. It was observed that the Ti-SBA-15 support, Fig. 1(a), was formed by grains of relatively uniform size (typically around 300 nm diameter and 700–1000 nm long). A well-ordered hexagonal array of mesopores can be seen for this sample. The Ti-SBA-16 material, Fig. 1(b), was formed by aggregates of spheroidal shape particles with some spaces between them. For the NT(3) and NT(5) materials, nanotubular structures can be clearly observed in Fig. 1(c) and (d). These open-ended structures with multilayered walls had the external diameter around 8–10 nm and internal pore diameter of around 3 and 5 nm, respectively.

Textural characteristics of the synthesized supports were determined by nitrogen physisorption. Fig. 2(a) shows nitrogen adsorption-desorption isotherms of the Ti-SBA-15 and Ti-SBA-16 supports. According to IUPAC classification, the Ti-SBA-15 support shows a type IV isotherm with a H1 hysteresis loop [22,24]. This hysteresis is characteristic of solids consisting of particles crossed by nearly cylindrical channels [28]. The Ti-SBA-15 material had a narrow monomodal pore size distribution centered on 78 Å, Fig. 3(a). The Ti-SBA-16 support also has a type IV isotherm, but with a H2 hysteresis loop, which is typical of ink-bottle pores of SBA-16 materials [15]. For the Ti-SBA-16 material, a bimodal pore size distribution was observed, Fig. 3(a). The first peak centered at 53 Å can be ascribed to the internal ink-bottle pores of the material, whereas the second one (at about 220 Å) can be attributed to the spaces between agglomerates of spheroidal particles forming SBA-16-type materials. Regarding two nanotubular titania supports NT(3) and NT(5), both of them show the typical type IV nitrogen adsorption isotherms, Fig. 2(b), with a noticeable hysteresis loop, which confirms the presence of meso- and macropores. The hysteresis profiles of NT materials can be interpreted as a combination of H1 and H3 types. Type H1 is characteristic of mesoporous materials having uniform nearly cylindrical channels; whereas H3 hysteresis is frequently associated with solids consisting of aggregates or agglomerates of particles forming slit shaped pores of non-uniform size [28]. Both nanotubular materials have bimodal pore size distributions with two principal signals, Fig. 3(b). For the NT(3) sample the first maximum was observed at around 30 Å, whereas the second broad peak had a maximum at 440 Å. The NT(5) material showed two broad peaks; the first one between 30 and 80 Å (the mean value around 50 Å) and the second at 700 Å. Considering that nanotubular titania supports are formed by aggregates or agglomerates of nanotubes, Fig. 1(c) and (d), the smaller pores can be ascribed to the pores inside the nanotubes, whereas larger pores can correspond to the voids in the aggregation of the nanotubes.

Textural characteristics of the synthesized supports (S_{BET} , S_{p} , V_{p} and D_{p}) are shown in Table 1. In general, the TiO_2 -containing supports of the SBA family had better textural characteristics (higher surface area and total pore volume) than the conventional γ -alumina. Contrary to all other supports, Ti-SBA-15 and Ti-SBA-16 showed the presence of a noticeable amount of micropores (98 and 62 m^2/g micropore area, respectively) in addition to larger mesopores. Nanotubular titania supports showed the BET surface areas slightly higher (238–258 m^2/g) than that of the conventional γ - Al_2O_3 support (216 m^2/g).

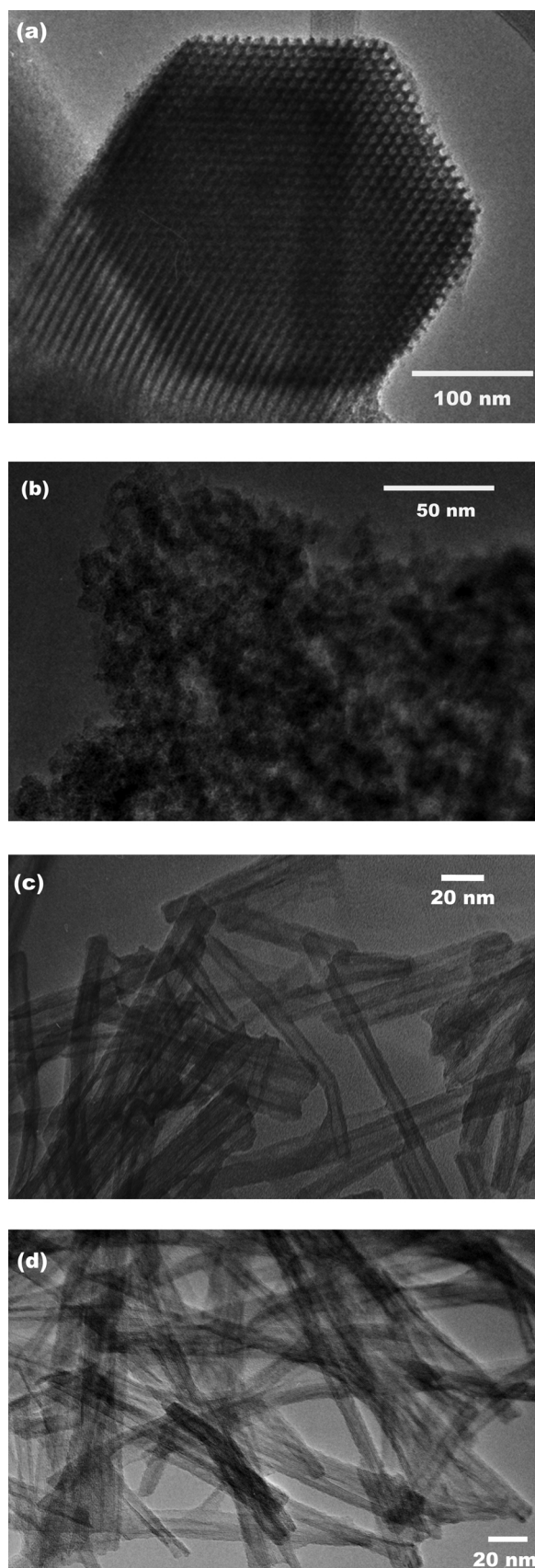


Fig. 1. TEM images of supports (a) Ti-SBA-15, (b) Ti-SBA-16, (c) NT(3) and (d) NT(5).

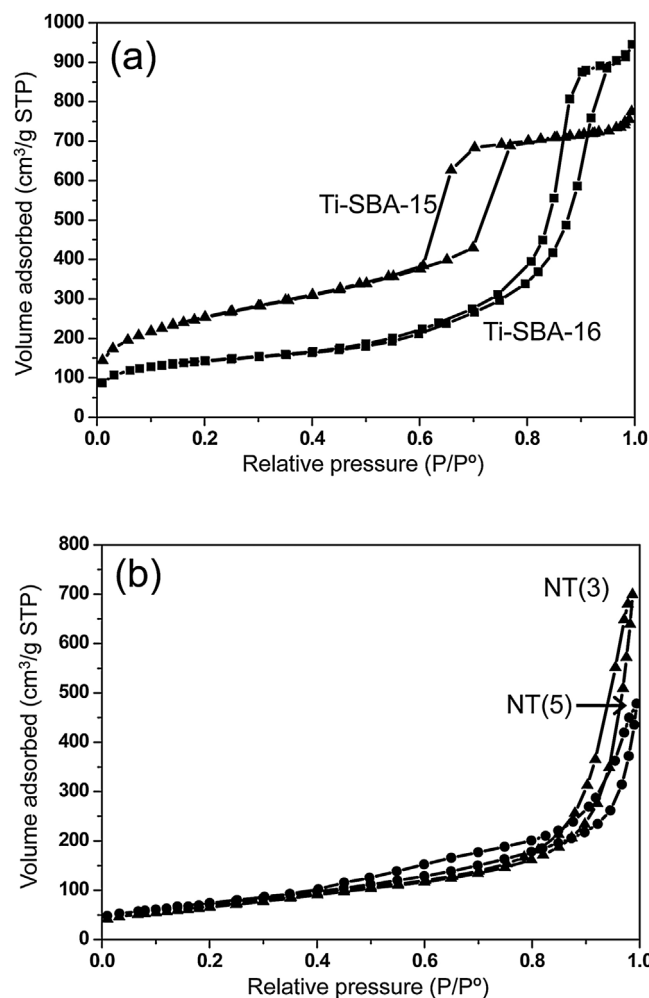


Fig. 2. Nitrogen adsorption–desorption isotherms of supports: (a) Ti-SBA-15 and Ti-SBA-16; (b) NT(3) and NT(5).

Fig. 4 shows the small-angle XRD patterns of the synthesized Ti-SBA-15 and Ti-SBA-16 samples. For the Ti-SBA-15 support with pore structure ordered in two dimensions (2D), three well-resolved peaks were observed: a very intense peak at about $1^\circ(2\theta)$ and two less intense signals at $1.7^\circ(2\theta)$ and $1.9^\circ(2\theta)$. These peaks can be assigned to (100), (110) and (200) reflections associated with $p6mm$ hexagonal symmetry of the SBA-15-type materials [22,23]. All three reflections yield a unit cell parameter (a_0) value of 105 Å, confirming that the measured structure is indeed of the $p6mm$ symmetry. Regarding the Ti-SBA-16 material, it has a three dimensional (3D) cubic pore arrangement. The XRD pattern of this material shows a strong reflection at about $0.9^\circ(2\theta)$ and two small should-

Table 1
Textural characteristics of supports.

Sample	S_{BET} (m^2/g) ^a	S_{μ} (m^2/g) ^b	V_p (cm^3/g) ^c	D_p (Å) ^d
Ti-SBA-15	636	98	0.83	78
Ti-SBA-16	521	62	1.43	53; 220
NT(3)	238	–	0.79	30; 440
NT(5)	258	–	0.49	50; 700
$\gamma\text{-Al}_2\text{O}_3$	216	–	0.52	109

^a Specific surface area calculated by BET method.

^b Micropore area estimated using the correlation of t -Harkins & Jura (t -plot method).

^c Total pore volume.

^d Pore diameter corresponding to the maximum of the pore size distribution calculated from the adsorption isotherm by the BJH method.

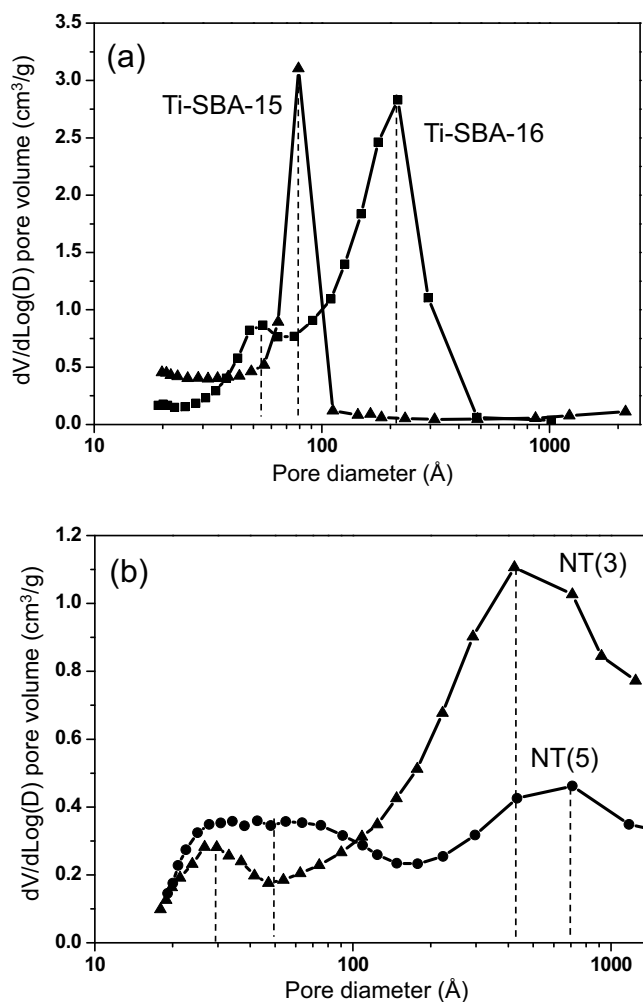


Fig. 3. Pore size distributions of supports: (a) Ti-SBA-15 and Ti-SBA-16; (b) NT(3) and NT(5).

ders at about $1.2^\circ(2\theta)$ and $1.5^\circ(2\theta)$. These signals correspond well to the (110), (200) and (211) reflections of the cubic $Im\bar{3}m$ structure of Ti-SBA-16 sample with a unit cell parameter (a_0) of 144 Å. Nanotubular titania materials NT(3) and NT(5) have a one dimensional nanostructure (1D), and because of this they do not present characteristic signals in the small-angle XRD region.

Powder XRD patterns of the synthesized supports and the reference $\gamma\text{-Al}_2\text{O}_3$ are shown in Fig. 5. It can be seen that the

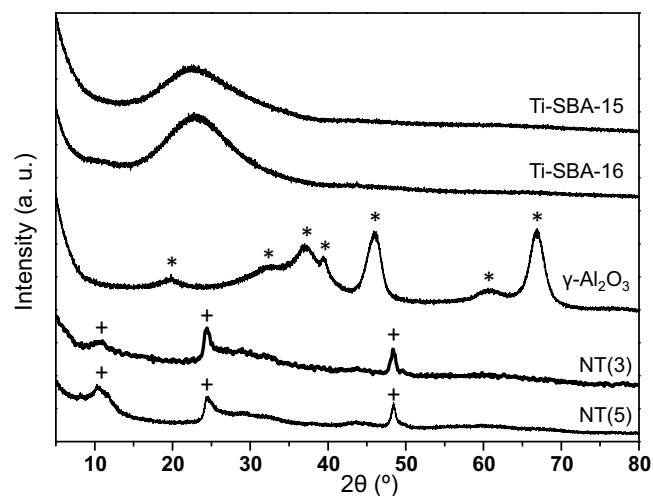


Fig. 5. Powder XRD patterns of supports: Ti-SBA-15, Ti-SBA-16, $\gamma\text{-Al}_2\text{O}_3$, NT(3) and NT(5). * $\gamma\text{-Al}_2\text{O}_3$ (JCPDS card 29-63), + $\text{H}_2\text{Ti}_3\text{O}_7$ (JCPDS card 41-192).

diffractograms of the Ti-containing SBA-15 and SBA-16 materials do not show the presence of any crystalline phase. A broad signal observed in these patterns between 15 and $35^\circ(2\theta)$ corresponds to the amorphous silica of the SBA-15 and SBA-16 supports. On the contrary, other three diffractograms show signals indicating that these materials have a crystalline structure. As expected, the alumina support had a $\gamma\text{-Al}_2\text{O}_3$ structure (JCPDS card 29-63). Nanotubular titania materials NT(3) and NT(5) showed similar X-ray diffraction patterns with three principal signals located at 11.2° , 24.4° and $48.4^\circ(2\theta)$. These reflections are typical of monoclinic layered trititanate phase ($\text{H}_2\text{Ti}_3\text{O}_7$, JCPDS card 41-192), which forms the curved nanotubular walls, and can be indexed to its (200), (110) and (020) crystal planes, respectively. The signal at $11.2^\circ(2\theta)$ is attributed to the interlayer distance of hydrogen trititanate which is equal to 8.0 Å. The broadness of all observed diffraction signals of NT(3) and NT(5) samples points out the poor crystalline nature of the synthesized nanotubes, which is in line with previous reports for similar materials [29,30].

Additional information about characteristics of titania species in different supports synthesized in the present work was obtained by UV–vis diffuse reflectance spectroscopy (Fig. 6). The DRS spectrum of the low-surface area titania used as precursor exhibits broad absorption at $\sim 330\text{ nm}$ with the absorption edge at about 380 nm due to ligand-to-metal charge transfer (LMCT) between the O^{2-} ligand and the titanium(IV) ion. This position of the absorption edge indicates that the TiO_2 precursor has a band-gap of ca.

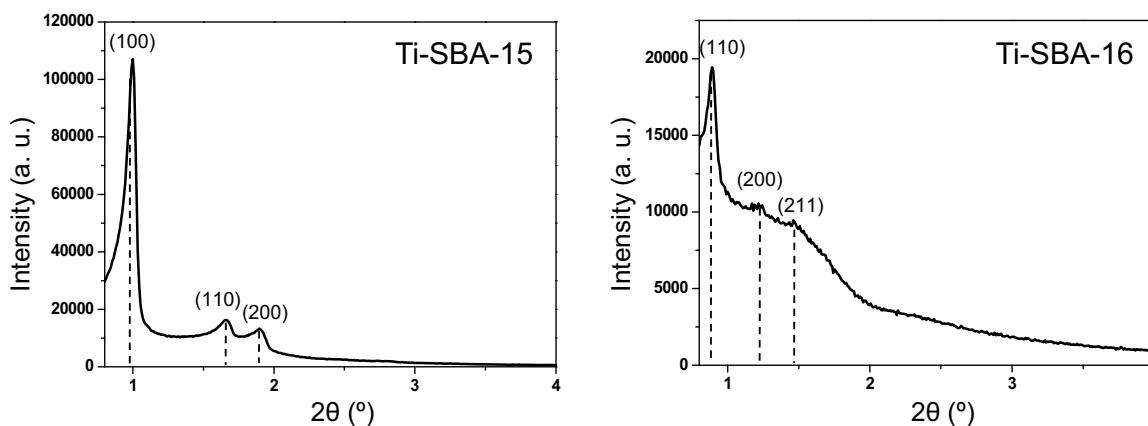


Fig. 4. Small-angle XRD patterns of Ti-SBA-15 and Ti-SBA-16.

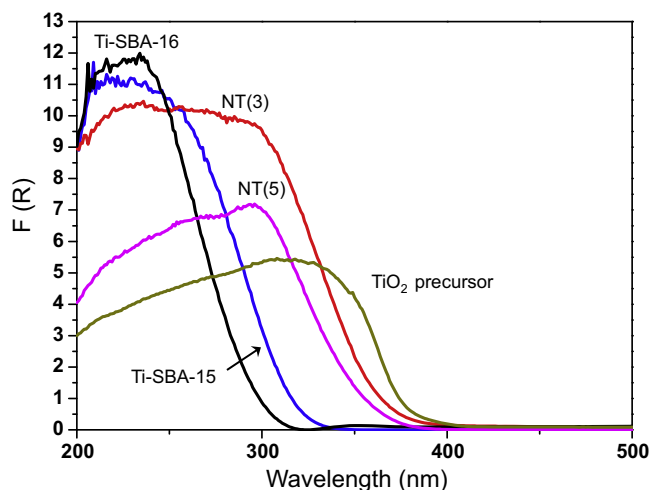


Fig. 6. UV-vis DRS supports: Ti-SBA-15, Ti-SBA-16, NT(3), NT(5) and low surface area TiO_2 anatase precursor.

3.3 eV, which is well in line with previous literature reports for the bulk TiO_2 anatase phase [31]. Transformation of the precursor TiO_2 into nanotubular titania structures NT(3) and NT(5) resulted in a blue shift of the absorption signals observed in the corresponding UV-vis DRS spectra (Fig. 6). Thus, the absorption band maximum was observed at about 300 nm for both nanotubular materials, whereas the absorption edge was located at 365 and 360 nm for NT(3) and NT(5), respectively, indicating an increase in the band-gap energy (E_g) of these materials to 3.4–3.5 eV. These differences in the electronic properties of the TiO_2 precursor and nanotubular titania samples can be attributed to a transformation of the bulk TiO_2 anatase into nano-sized titania structures (titania nanotubes) [31,32]. In the DRS spectra of Ti-SBA-15 and Ti-SBA-16 further blue shift can be observed; the absorption band maxima are located at about 230 nm and the absorption edge at 320 and 300 nm, respectively. These Ti-containing samples of the SBA-family prepared by chemical grafting of TiO_2 species had still higher E_g values (3.9 eV for Ti-SBA-15 and 4.1 eV for Ti-SBA-16). Previously, the band at 230 nm was assigned to LMCT transitions involving isolated Ti atoms in tetrahedral coordination [33]. In addition, in the spectrum of the Ti-SBA-15 sample a shoulder can be observed at about 250 nm, which indicates the presence of some isolated octahedral Ti species [16,33]. Therefore, the DRS characterization of the

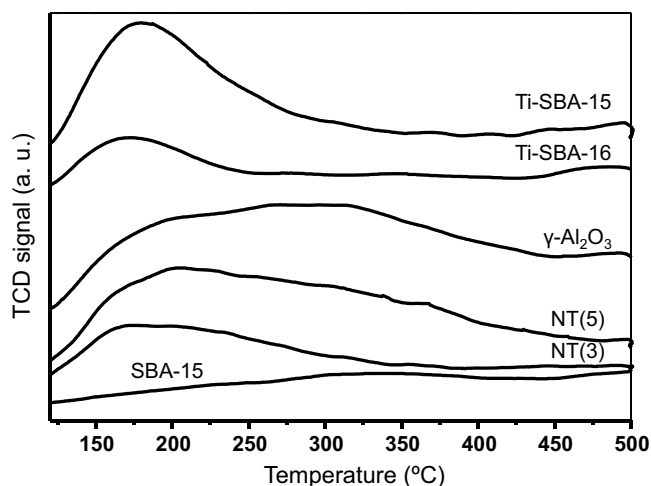


Fig. 7. Ammonia TPD profiles of supports (Ti-SBA-15, Ti-SBA-16, $\gamma\text{-Al}_2\text{O}_3$, NT(5) and NT(3)) and parent SBA-15 material.

Table 2
Quantitative analysis of ammonia TPD results obtained for supports.

Sample	Amount of acid sites ($\mu\text{mol NH}_3/\text{g}$)			
	Total	Weak (120–200 °C)	Medium (200–400 °C)	Strong (400–500 °C)
SBA-15	188	13	99	76
Ti-SBA-15	336	161	147	28
Ti-SBA-16	204	88	63	53
NT(3)	512	129	280	103
NT(5)	533	109	314	110
$\gamma\text{-Al}_2\text{O}_3$	728	100	381	247

synthesized supports revealed the differences in the type of titania species in them; namely, in the NT(3) and NT(5) samples, nano-sized titania species were found, whereas in the Ti-SBA-15 and Ti-SBA-16 samples, only isolated Ti species were present.

Ammonia TPD characterization results are shown in Fig. 7 and Table 2. Pure silica SBA-15 material used for the preparation of the Ti-SBA-15 support has the lowest total amount of acid sites among all samples. Titania grafting on this material resulted in an increase in the total amount of acid sites, especially of the weak and medium strength ones, and a slight decrease in the amount of strong acid sites. Similar distribution of acid sites of different strength was also observed for the Ti-SBA-16 support, presenting mostly weak and medium acid sites. Alike acid characteristics of the above two materials (Ti-SBA-15 and Ti-SBA-16) should be due to the presence of similar titania species in them, namely isolated tetrahedral and octahedral Ti oxide species detected by DRS. The principal difference between these materials is a larger total amount of acid sites in the Ti-SBA-15 sample compared to the Ti-SBA-16 analog, which can be ascribed to a larger amount of titania grafted in the first case (16 wt.% of TiO_2 for Ti-SBA-15 versus 14 wt.% for Ti-SBA-16). Nanotubular titania supports NT(3) and NT(5), showed a significantly larger acidity than the SBA-based materials (Fig. 7, Table 2). Thus, the total amount of acid sites in NT(3) and NT(5) was almost twice higher than in the Ti-SBA samples. In addition, medium strength sites were predominant in both cases in line with the presence of a noticeable amount of weak and strong acid sites. These acid characteristics can be due to the presence of nano-sized titania species in the nanotubular supports. However, in general, acidity of the nanotubular titania supports was smaller than that of the reference γ -alumina support, which showed the highest total amount of acid sites as well as of medium and strong acid sites among all supports tested.

The above differences in the characteristics of the titania species in different supports are expected to affect the supports' interaction with the deposited Ni and Mo species and their catalytic activity.

3.2. Catalysts

Impregnation of Ni and Mo species on the Ti-containing supports, Ti-SBA-15, Ti-SBA-16, NT(3) and NT(5) did not produce significant changes in the characteristic shape of the isotherms, which confirms that the original pore structure of the supports was preserved in the NiMo catalysts. As expected, for all catalysts the amount of adsorbed nitrogen as well as specific textural characteristics (S_{BET} and V_p , Table 3) decreased after metal deposition. However, this decrease was much stronger for the catalysts supported on Ti-SBA-15 and Ti-SBA-16 materials than for other supports. Thus, surface area and pore volume values of the NiMo/Ti-SBA-15 and NiMo/Ti-SBA-16 catalysts were about ~30–40% smaller than those of the corresponding supports (Tables 1 and 3). This decrease is much larger than the increase in the sample's density (about 18%) after the deposition of metal species. This can be due to the deposition of the impregnated metal species inside the

Table 3
Textural characteristics of NiMo catalysts.

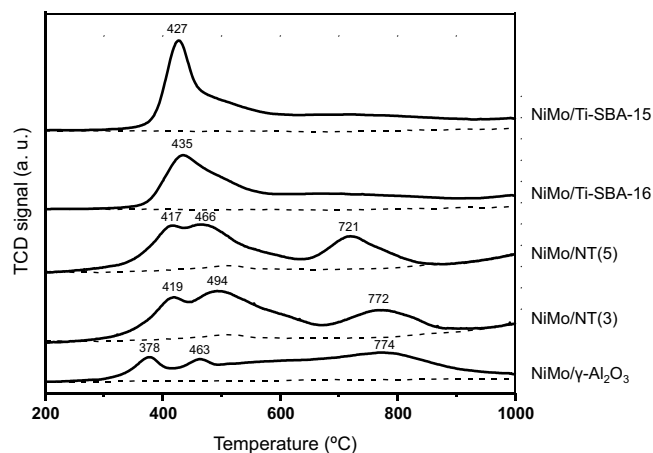
Sample	S_{BET} (m ² /g) ^a	S_{μ} (m ² /g) ^b	V_p (cm ³ /g) ^c	D_p (Å) ^d
NiMo/Ti-SBA-15	435	60	0.61	76
NiMo/Ti-SBA-16	289	200	0.94	53; 210
NiMo/NT(3)	209	–	0.72	30; 430
NiMo/NT(5)	207	–	0.40	50; 640
NiMo/ γ -Al ₂ O ₃	178	–	0.40	100

^a Specific surface area calculated by BET method.^b Micropore area estimated using the correlation of *t*-Harkins & Jura (*t*-plot method).^c Total pore volume.^d Pore diameter corresponding to the maximum of the pore size distribution calculated from the adsorption isotherm by the BJH method.

mesopores of the SBA-family supports, which is in line with the incipient wetness impregnation method used for the catalysts' preparation. In addition, some agglomeration of the deposited Ni and Mo oxide species can also take place inside the pores leading to a blocking of mesopore channels. As a comparison, for the NiMo catalysts supported on NT(3) and NT(5), a decrease in the textural characteristics was just about 12–19% in reference to the corresponding supports. Therefore, for the last two catalysts, no agglomeration of the deposited Ni and Mo oxide species was expected.

Small-angle XRD patterns of the NiMo catalysts supported on Ti-SBA-15 and Ti-SBA-16 materials were similar to those shown in Fig. 4 for the corresponding supports. The position of the reflections characteristic of Ti-SBA-15 and Ti-SBA-16 and their intensities almost did not change after the impregnation of Ni and Mo, indicating that the long-range periodicity order of the 2D and 3D SBA-family supports was preserved in the prepared catalysts and their unit-cell parameters did not suffer a significant change after metal deposition.

Powder X-ray diffraction patterns of the NiMo catalysts prepared in the present work were recorded in the 2θ range from 5° to 80°. No signals attributable to the presence of any new crystalline phase (MoO₃, NiO, NiMoO₄, etc.) were detected in the XRD pattern of any catalyst. Only reflections corresponding to the supports (Fig. 5) were observed. This result points out to a good dispersion of the deposited metal oxide species in all prepared catalysts.

**Fig. 8.** TPR profiles of the NiMo catalysts supported on different materials (solid lines). TPR profiles of the corresponding supports are shown as dashed lines below the reduction profiles of the catalysts.

Results from the TPR characterization of the synthesized NiMo catalysts supported on Ti-SBA-15, Ti-SBA-16, NT(3), NT(5) and γ -alumina are shown in Fig. 8. TPR profiles of the corresponding supports are also shown for comparison (dashed lines). It can be seen that the obtained TPR profile (number of reduction peaks, position and intensity) strongly depends on the support used. Thus, for the reference NiMo/ γ -Al₂O₃ catalyst, three reduction peaks can be observed at 378, 463 and 774 °C. According to literature [34,35], hydrogen consumption in the low temperature region (300–500 °C) can be attributed to the first step of reduction (from Mo⁶⁺ to Mo⁴⁺) of octahedral Mo oxide species, Mo(OH), of different degrees of agglomeration. An increase in the degree of agglomeration of octahedral Mo oxide species is accompanied by an increase in reduction temperature. In addition, the signal with the maximum at 463 °C can be ascribed to the reduction of the NiMoO₄ species (main peak at 475 °C [36]). The formation of these species can be expected in our catalysts, since they were prepared by the co-impregnation of Ni and Mo precursor species, which favor the formation of an Anderson-type heteropolymolybdate

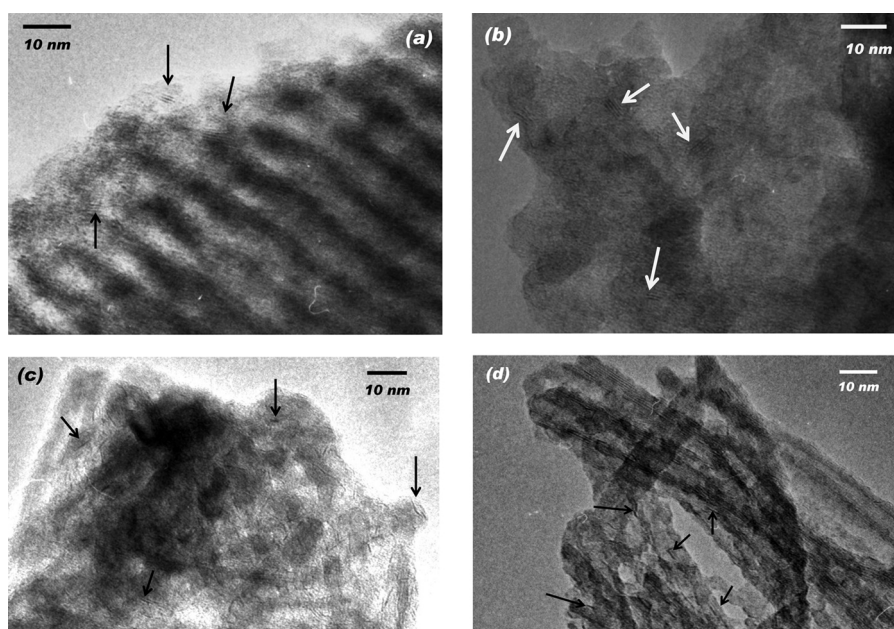
**Fig. 9.** HRTEM of sulfided catalysts: (a) NiMo/Ti-SBA-15, (b) NiMo/Ti-SBA-16, (c) NiMo/NT(3) and (d) NiMo/NT(5).

Table 4
Reduction behavior of different NiMo catalysts.

Sample	H ₂ consumption (mmol/g) ^a			α_R ^b
	200–600 °C	600–1000 °C	Total	
NiMo/Ti-SBA-15	1.51	0.80	2.31	0.80
NiMo/Ti-SBA-16	1.48	0.97	2.45	0.84
NiMo/NT(3)	1.66	1.11	2.77	0.96
NiMo/NT(5)	1.78	0.96	2.74	0.94
NiMo/ γ -Al ₂ O ₃	0.98	1.29	2.27	0.78

^a Hydrogen consumption determined from TPR results: H₂ consumptions due to the supports' reduction were subtracted from the H₂ consumptions of the corresponding catalysts.

^b α_R , degree of the reduction of Ni and Mo oxide species determined from total H₂ consumption of each sample and the theoretical value corresponding to their complete reduction (2.90 mmol/g).

(NH₄)₄[Ni(OH)₆Mo₆O₁₈]·4H₂O in the impregnation solution [37], which precipitates on the support surface and upon calcination yields the NiMoO₄ phase. Hydrogen consumption at a higher temperature (500–700 °C) can be ascribed to the second step of reduction of Mo(OH) species (from Mo⁴⁺ to Mo⁰) and to the first step of reduction of small MoO₃ clusters. Finally, the signal observed in the 700–1000 °C region corresponds to the first step of reduction of tetrahedral Mo oxide species, Mo(Td), being in strong interaction with the support. Therefore, the TPR results show that the NiMo/ γ -Al₂O₃ catalyst has both types of Mo oxide species, octahedral and tetrahedral, with a considerable contribution of the Mo(Td) species reducible at a high temperature. The TPR profiles of the NiMo catalysts supported on nanotubular titania materials, NT(3) and NT(5) (Fig. 8), also exhibit three main reduction peaks: the first intense signal with the maximum at 417–419 °C, the second similar intensity peak at a higher temperature (466–494 °C) and the last signal in the temperature interval between 650 and 900 °C. The TPR profiles of the NiMo/Ti-SBA-15 and NiMo/Ti-SBA-16 catalysts (Fig. 8) presented the principal reduction signal at about 430 °C with a shoulder at about 500 °C and a low-intensity hydrogen consumption at a 600–1000 °C interval. The TPR profiles of the catalysts supported on Ti-containing materials of the SBA-family showed clearly that octahedral Mo oxide species are predominant in these two samples. It seems that the type of Mo species in NiMo catalysts is related to the characteristics of the titania species in the supports. Isolated, low acidity Ti moieties (Ti-SBA-15 and Ti-SBA-16 supports) result in dispersed octahedral Mo species, while an increase in the supports' acidity (NT(3) and NT(5) supports) leads to an increase in the proportion of tetrahedral ones.

In addition, hydrogen consumption and degree of reduction (α_R) were determined for different NiMo catalysts (Table 4). In order to quantify the amount of metal species that can be reduced at low and high temperatures, hydrogen consumption in two temperature intervals (200–600 °C and 600–1000 °C) was also determined (Table 4). The NiMo catalysts supported on Ti-SBA-15, Ti-SBA-16 and γ -Al₂O₃ showed similar degrees of reduction ($\alpha_R \sim 0.8$). However, the catalysts supported on SBA-type materials showed higher hydrogen consumption at a lower-temperature interval (200–600 °C) than the alumina-supported NiMo sample. This indicates that Ni and Mo oxide species can be reduced more easily when supported on SBA-type materials than on γ -alumina. Regarding the NiMo catalysts supported on nanotubular titania materials, NT(3) and NT(5), they showed a higher degree of reduction (α_R 0.94–0.96) than the other three catalysts, as well as higher hydrogen consumption at a low-temperature interval.

HRTEM characterization of sulfided NiMo catalysts was performed in order to obtain information about the dispersion of catalytically active MoS₂ species. Fig. 9 shows HRTEM micrographs of the NiMo catalysts supported on different titania-containing materials. The typical fringes of MoS₂ crystallites with 0.61 nm

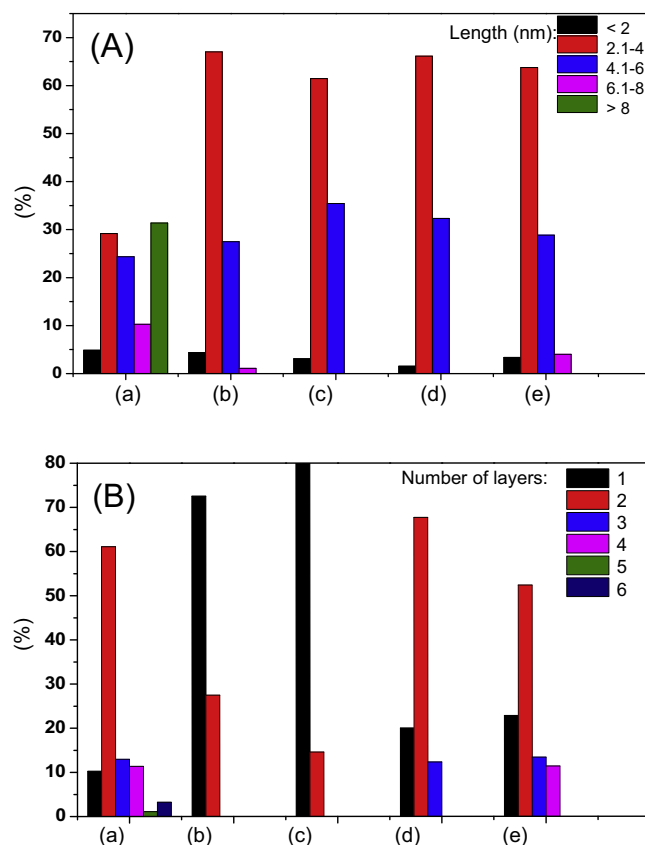


Fig. 10. Length (A) and stacking (B) distributions of MoS₂ crystallites in sulfided catalysts: (a) NiMo/ γ -Al₂O₃, (b) NiMo/NT(3); (c) NiMo/NT(5), (d) NiMo/Ti-SBA-15 and (e) NiMo/Ti-SBA-16.

interplanar distances were observed on micrographs of all sulfided catalysts. In general, MoS₂ particles observed in the Ti-SBA-15 and Ti-SBA-16-supported catalysts had similar morphology (images (a) and (b), Fig. 9). They were formed by 1–4 layers with lengths between 2 and 8 nm. Regarding the NiMo catalysts supported on two nanotubular titania materials, they showed mainly the presence of the active phase particles of just 1 or 2 layers with less than 6 nm length (images (c) and (d), Fig. 9). In this case, we also did not observe a noticeable difference in the characteristics of the sulfided MoS₂ particles deposited on NT materials of different internal pore diameter. The above results indicate that the characteristics of the deposited MoS₂ crystallites were influenced principally by the chemical composition of the supports (TiO₂-SiO₂ for Ti-SBA-15 and Ti-SBA-16, or H₂Ti₃O₇ for NT(3) and NT(5)), whereas the shape and size of the pores and other textural characteristics of the supports did not have a strong influence on the stacking degree and length of the MoS₂ particles. Fig. 10 shows the stacking and length distributions of MoS₂ crystallites in the sulfided catalysts supported on Ti-SBA-15, Ti-SBA-16, NT(3) and NT(5), where the differences in the morphology of the MoS₂ phase can be observed in a more detailed way. The information regarding the reference NiMo/ γ -Al₂O₃ catalysts was also included for comparison purposes. The reference catalyst showed broad length and stacking distributions. At the same time, in the Ti-SBA-15 and Ti-SBA-16-supported samples, MoS₂ particles of 2 layers and 2–4 nm in length were predominant. For the NiMo catalysts supported on nanotubular titania materials, the majority of the MoS₂ particles had just 1 layer and 2–4 nm in length. It seems that a stronger metal-support interaction on NT supports resulted in less stacked MoS₂ particles than on Ti-SBA materials. Therefore, the use of Ti-containing supports allowed us

Table 5

Results from the characterization of the sulfided NiMo catalysts by HRTEM: average length (L) and average stacking degree (N) of MoS_2 crystallites and estimated f_{Mo} fraction.^a

Catalyst	L (Å)	N	f_{Mo}
NiMo/Ti-SBA-15	36	1.9	0.32
NiMo/Ti-SBA-16	36	2.1	0.32
NiMo/NT(3)	35	1.3	0.33
NiMo/NT(5)	35	1.2	0.33
NiMo/ γ - Al_2O_3	80	2.4	0.15

^a f_{Mo} , estimated fraction of Mo atoms on the edge surface of MoS_2 crystallites [37,38].

to improve the dispersion of the active phase in the sulfided catalysts. The above observations were confirmed by the calculation of the average length (L) and number of layers (N) of MoS_2 crystallites in different catalysts (Table 5). These average characteristics were used to estimate the fraction of Mo atoms (f_{Mo}) located on the edge surface of MoS_2 crystallites. The f_{Mo} fraction was calculated using equations reported in [38,39], assuming that the MoS_2 crystallites are perfect hexagons. This fraction can be considered as an indica-

tor of the amount of sulfided Mo species located on the catalytically active surface of MoS_2 particles [40]. The results from Table 5 show that the f_{Mo} values found for all NiMo catalysts supported on SBA-type materials and titania nanotubes were similar (~ 0.3) and twice higher than that of the reference NiMo/ γ - Al_2O_3 sample ($f_{\text{Mo}} = 0.15$). Therefore, in spite of the difference in the average stacking degree (N , Table 5) of the SBA- and NT-supported catalysts, all four catalysts supported on Ti-containing materials possess almost the same amount of catalytically active sites, available for interaction with reactant molecules.

3.3. Catalytic behavior in hydrodesulfurization

In the present study, the catalytic activity of the NiMo catalysts was tested in simultaneous hydrodesulfurization (HDS) of dibenzothiophene (DBT) and 4,6-dimethyldibenzothiophene (4,6-DMDBT). These two sulfur-containing molecules were selected as representatives of the refractory sulfur compounds contained in the diesel fraction of petroleum [41]. Tables 6 and 7 show DBT and 4,6-DMDBT conversions obtained with the synthesized NiMo catalysts at different reaction times. Results obtained with

Table 6

Activity and selectivity of different NiMo catalysts in hydrodesulfurization of DBT.

Catalyst	DBT conversion (%) ^a				k_{DBT} (h^{-1}) ^b	$k_{\text{DBT}} \times 10^5$ ($\text{L s}^{-1} \text{g}_{\text{cat}}^{-1}$)	CHB/BP ^c
	2 h	4 h	6 h	8 h			
NiMo/Ti-SBA-15	46	72	86	94	0.29	2.15	1.22
NiMo/Ti-SBA-16	36	65	85	95	0.24	1.79	1.52
NiMo/NT(3)	40	68	90	96	0.28	2.07	1.14
NiMo/NT(5)	33	60	85	94	0.22	1.61	1.21
NiMo/ γ - Al_2O_3	36	66	83	93	0.25	1.85	0.39

CHB, cyclohexylbenzene; BP, biphenyl.

^a DBT conversion at different reaction times.

^b k_{DBT} , overall pseudo-first order rate constants determined from linear plots shown in Fig. 11(a).

^c Ratio of the principal reaction products at 50% of DBT conversion.

Table 7

Activity and selectivity of different NiMo catalysts in hydrodesulfurization of 4,6-DMDBT.

Catalyst	4,6-DMDBT conversion (%) ^a				k_{DMDBT} (h^{-1}) ^b	$k_{\text{DMDBT}} \times 10^5$ ($\text{L s}^{-1} \text{g}_{\text{cat}}^{-1}$)	MCHT/DMBP ^c
	2 h	4 h	6 h	8 h			
NiMo/Ti-SBA-15	33	56	74	88	0.18	1.33	8.67
NiMo/Ti-SBA-16	26	51	75	90	0.17	1.22	8.26
NiMo/NT(3)	27	53	80	94	0.16	1.16	2.97
NiMo/NT(5)	24	44	73	89	0.14	1.04	3.63
NiMo/ γ - Al_2O_3	13	26	40	53	0.07	0.54	9.46

MCHT, methylcyclohexyltoluene; DMBP, dimethylbiphenyl.

^a 4,6-DMDBT conversion at different reaction times.

^b k_{DMDBT} , overall pseudo-first order rate constants determined from linear plots shown in Fig. 11(b).

^c Ratio of the principal reaction products at 50% of 4,6-DMDBT conversion.

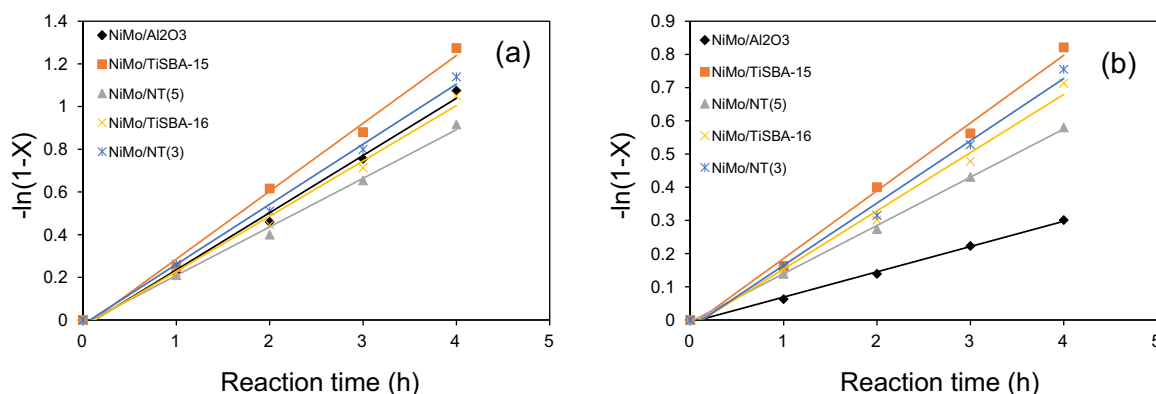


Fig. 11. Pseudo-first-order kinetics linear plots for (a) DBT HDS and (b) 4,6-DMDBT HDS.

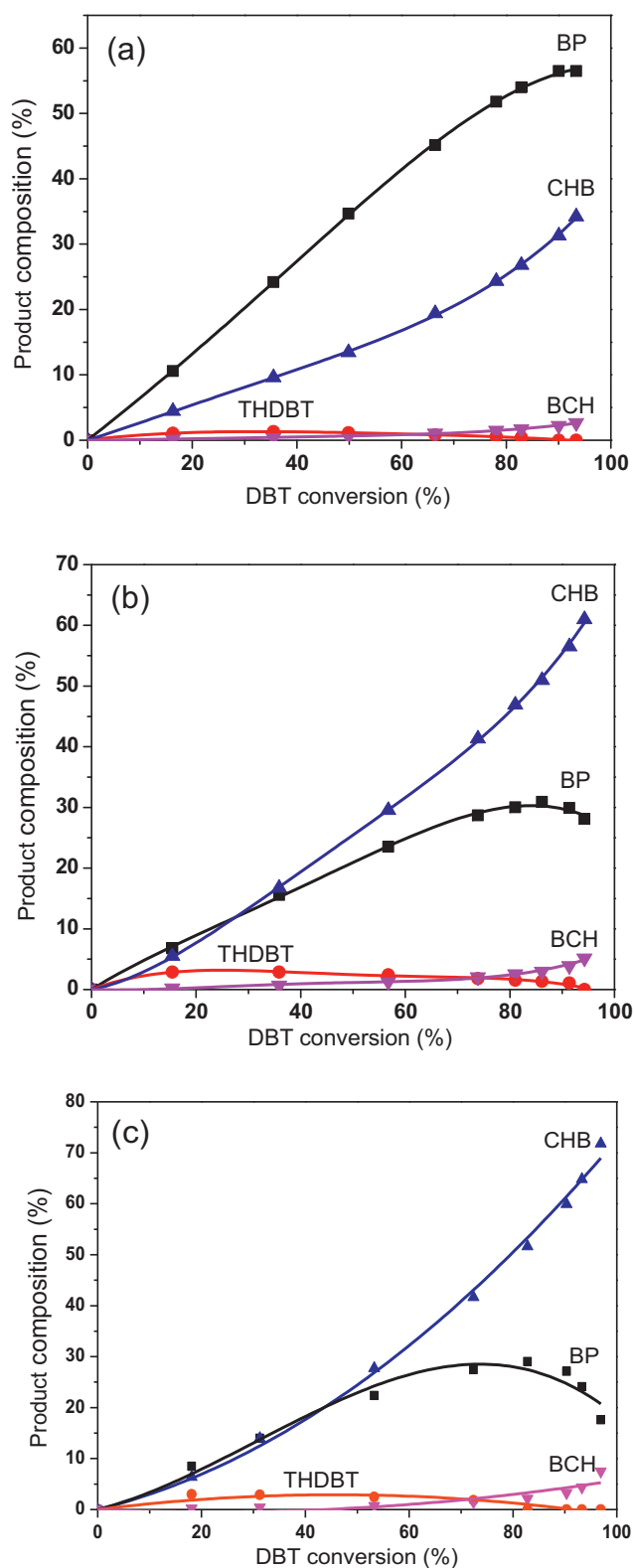


Fig. 12. Product compositions obtained in HDS of DBT over NiMo catalysts: (a) NiMo/ γ -Al₂O₃, (b) NiMo/Ti-SBA-15 and (c) NiMo/NT(3). Detected products: BP, biphenyl; CHB, cyclohexylbenzene; BCH, bicyclohexyl; THDBT, tetrahydrodibenzothiophene.

the reference NiMo/ γ -Al₂O₃ catalyst are also included. In general, DBT conversions reached with all catalysts (Table 6) were higher than those of 4,6-DMDBT (Table 7). This is in line with the well-known fact that dibenzothiophene molecules with alkyl groups in positions 4 and 6 are less reactive and more difficult to eliminate by HDS than unsubstituted DBT [42,43]. The reference NiMo/ γ -Al₂O₃ catalyst resulted in 93% of DBT conversion and 53% of 4,6-DMDBT at 8 h reaction time. This low catalytic activity for the hydrodesulfurization of 4,6-dimethyldibenzothiophene is a particular characteristic of the alumina-supported NiMo catalysts. It can be noted in Table 6 that the NiMo/Ti-SBA-15 and NiMo/NT(3) catalysts showed slightly higher catalytic activity in DBT HDS than the γ -alumina-supported reference and two other catalysts tested. The pseudo-first-order rate constants calculated for HDS of DBT with two more active catalysts were also slightly higher (12–15%) than that of the NiMo/ γ -Al₂O₃ (Fig. 11(a), Table 6). The above activity results show that change in the support nature does not have strong implications on the activity of the NiMo catalysts in the hydrodesulfurization of DBT. In contrast, in the HDS of 4,6-DMDBT, all NiMo catalysts supported on Ti-containing materials showed noticeably improved catalytic activity than the reference NiMo/ γ -Al₂O₃ sample (Fig. 11(b), Table 7). In this case, 4,6-DMDBT conversions of 88–94% were reached at 8 h. The pseudo-first-order rate constants calculated for HDS of 4,6-DMDBT with the NiMo catalysts supported on Ti-containing SBA materials were slightly higher than those calculated for the catalysts supported on NT(3) and NT(5). Nevertheless, all these constants were significantly higher (1.8–2.5 times) than that of the NiMo/ γ -Al₂O₃ (Table 7). In addition, the pseudo-first-order rate constants determined in the present work for simultaneous HDS of DBT and 4,6-DMDBT are similar to those reported by us previously for HDS of DBT in the presence of the NiMo catalyst supported on low-sodium titania nanotubes ($1.85 \times 10^{-5} \text{ L s}^{-1} \text{ g}_{\text{cat}}^{-1}$, [46]) and for HDS of 4,6-DMDBT with NiMo/Ti-SBA-15 ($\sim 1 \times 10^{-5} \text{ L s}^{-1} \text{ g}_{\text{cat}}^{-1}$, [16]). That means that the catalytic behavior of these catalysts is almost not affected by the presence of different types of DBT molecules in the reaction mixture. The NiMo/Ti-SBA-15 sample showed the highest catalytic activity (highest values of k_{DBT} and k_{DMDBT} , Tables 6 and 7) among all NiMo catalysts tested. Probably, this can be attributed to the fact that this catalyst has the highest amount of dispersed octahedral Mo oxide species easy to be reduced at low temperature (TPR, Fig. 8) leading to the formation of well-sulfided and dispersed MoS₂ active species (Table 5). It seems that the amount of Ti species loaded to this support and their characteristics (isolated Ti species) provide an optimal metal-support interaction with the deposited Ni and Mo oxide species. It is worth mentioning that all NiMo catalysts prepared in the present work using Ti-containing materials of different types resulted in high conversions of both DBT and 4,6-DMDBT molecules, in contrast to the NiMo/ γ -Al₂O₃ reference. Thus, DBT conversions of 94–96% and 4,6-DMDBT conversions of 88–94% were obtained with these catalysts at 8 h reaction time. From the above results it can be clearly observed that (i) the NiMo catalysts supported on Ti-containing materials (Ti-SBA-15, Ti-SBA-16, NT(3) and NT(5)) were significantly more active for HDS of 4,6-DMDBT than the alumina-supported reference, and (ii) the NiMo/Ti-SBA-15 catalyst showed the highest catalytic activity for HDS of both S-containing molecules tested.

It is well-known that the hydrodesulfurization of DBT-type molecules occurs through two parallel reaction routes, namely, (i) direct desulfurization (DDS) yielding the corresponding biphenyl-type products, and (ii) hydrogenation with subsequent desulfurization (HYD), leading first to the pre-hydrogenated intermediates (tetrahydro- and hexahydrodibenzothiophenes) and then to cyclohexylbenzene-type compounds [44,45]. The main reaction product obtained in the HDS of dibenzothiophene through the DDS route is biphenyl (BP), whereas through the

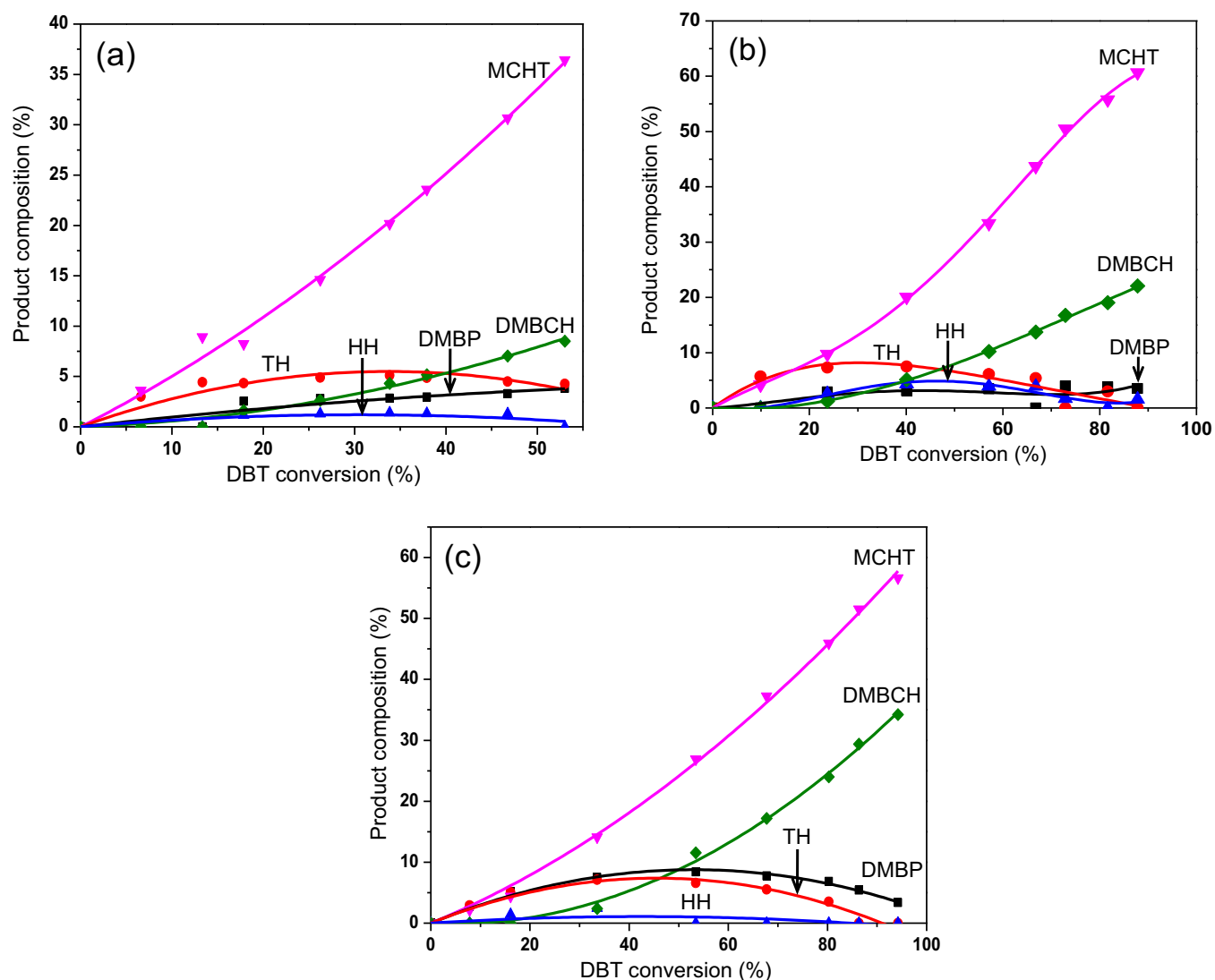


Fig. 13. Product compositions obtained in HDS of 4,6-DMDBT over NiMo catalysts: (a) NiMo/ γ -Al₂O₃, (b) NiMo/Ti-SBA-15 and (c) NiMo/NT(3). Detected products: DMBP, dimethylbiphenyl; MCHT, methylcyclohexyltoluene; DMDBCH, dimethylbicyclohexyl; TH, tetrahydrodimethyldibenzothiophene; HH, hexahydrodimethyldibenzothiophene.

HYD route it is cyclohexylbenzene (CHB). For the HDS of 4,6-dimethyldibenzothiophene, the corresponding products are dimethylbiphenyl (DMBP) and methylcyclohexyltoluene (MCHT). Tables 6 and 7 show the ratios of the main desulfurized products (CHB/BP and MCHT/DMBP) obtained with different catalysts in HDS of DBT and 4,6-DMDBT, respectively. These ratios were determined at 50% of DBT or 4,6-DMDBT conversion and can be used as a measure of the catalyst's selectivity. The NiMo catalyst supported on alumina showed low cyclohexylbenzene to biphenyl ratio (0.39, Table 6). The main desulfurized product obtained with this catalyst in the HDS of DBT was biphenyl (BP), which points out that the DDS pathway of the reaction was the predominant reaction route. This conclusion can be confirmed by the selectivity curve shown in Fig. 12(a), for this catalyst, where it can be seen that BP is the main product for all DBT conversions shown. For the NiMo catalysts supported on different Ti-containing materials, CHB/BP ratios from 1.14 to 1.52 were obtained at 50% of DBT conversion (Table 6), indicating that all these catalysts have higher hydrogenation ability than that of the NiMo/ γ -Al₂O₃ reference. At DBT conversions higher than 45–50%, CHB became the main product obtained with these catalysts (Fig. 12(b) and (c)).

Regarding the product distributions obtained for the hydrodesulfurization of 4,6-DMDBT (Fig. 13), methylcyclohexyltoluene (MCHT) was the principal desulfurized product obtained with all NiMo catalysts tested. This is in line with the well-known preference of this molecule for the HYD pathway of HDS, which, in general, is attributed to the presence of alkyl groups in positions 4 and 6 of the molecule strongly blocking the hydrogenolysis (DDS) pathway [43]. In this case, the hydrogenation ability of the catalysts (MCHT/DMBP ratio, Table 7) increases in the following order: NiMo/NT(3) < NiMo/NT(5) < NiMo/Ti-SBA-16 < NiMo/Ti-SBA-15 < NiMo/ γ -Al₂O₃. In general, a strong difference (of about 3 times) was observed in the MCHT/DMBP ratios obtained with different catalysts. Thus, the amount of MCHT obtained with the NiMo/NT(3) and NiMo/NT(5) catalysts at 50% of 4,6-DMDBT conversion was 3–4 times larger than the amount of DMBP. Under the same conditions, Ti-SBA-15 and Ti-SBA-16-supported catalysts, as well as the NiMo/ γ -Al₂O₃ reference, resulted in the formation of a much larger proportion of MCHT product and only a small amount of DMBP (MCHT/DMBP ratios ~8.3–9.5, Table 7). No clear relationship was observed between the hydrogenation ability of the catalysts (MCHT/DMPB ratio) and their activity

in HDS of 4,6-DMDBT. Thus, the NiMo/NT(3) and NiMo/NT(5) catalysts showed high activity in line with a significantly lower MCHT/DMBP ratio than all other catalysts. This is an interesting result, since the majority of the catalysts active for the HDS of 4,6-DMDBT have high hydrogenation ability, which is normally related to morphological characteristics, principally stacking degree, of the MoS₂ active phase. Thus, in general, it is considered that HYD rates increase with an increasing stacking degree attributed to a less hampered planar adsorption geometry of reactants on multilayered MoS₂ crystallites [40]. In our previous works, it was found that high activity for the HDS of 4,6-DMDBT is normally obtained with the catalysts having well dispersed short (3–4 nm) MoS₂ particles formed by 2–3 layers [15,16,39]. On the other hand, a decrease in the stacking degree of the MoS₂ clusters in general resulted in an increase in the selectivity of the catalysts toward the DDS route of HDS, and diminishing of the overall catalytic activity in HDS of refractory alkyl-substituted dibenzothiophenes, such as 4,6-DMDBT. In the present work, we found for the first time that the NiMo/NT(3) and NiMo/NT(5) catalysts are able to desulfurize efficiently 4,6-DMDBT, not only through the HYD pathway, but also through the DDS route of the reaction. We think that this unusual catalytic behavior of the NiMo/NT catalysts is due to high dispersion of the MoS₂ active phase and the particular morphology of the used nanotubular titania support. It's possible that the use of this material and its surface curvature helps to diminish steric hindrance problems, thus allowing the plug-in adsorption of 4,6-DMDBT molecules on the hydrogenolysis active sites of low-stacked MoS₂ active phase. It should be mentioned that recently, similar results have been obtained in ultra-deep hydrodesulfurization with the NiW catalyst supported on 1D γ -Al₂O₃ nanorods [47]. This catalyst showed higher catalytic activity for HDS of both DBT and 4,6-DMDBT than the reference NiWP/ γ -Al₂O₃ commercial catalyst and unexpectedly high hydrogenolysis ability in HDS of 4,6-DMDBT (the DDS rate with this catalyst was twice larger than the obtained with the NiWP/ γ -Al₂O₃ reference). It was also observed that the NiW catalyst supported on 1D γ -Al₂O₃ nanorods was formed by short (~1.9 nm) and low-stacked (1–2 layers) sulfide species which were able to desulfurize 4,6-DMDBT through both the HYD and the DDS routes of the reaction. Based on theoretical calculations, the authors supposed that this behavior is due to the fact that Ni–W–S sites on small slabs could act as hydrogenolysis sites rather than as hydrogenation sites.

4. Conclusions

In the present work, NiMo catalysts supported on four different titania-containing materials were synthesized, characterized and tested in the hydrodesulfurization of dibenzothiophene-type compounds. Among the used supports were 2D and 3D nanostructured materials of the SBA-family modified with titania by chemical grafting (Ti-SBA-15 and Ti-SBA-16, respectively), as well as 1D titania nanotubes of different pore diameters. For comparison purposes, a NiMo/ γ -Al₂O₃ catalyst was also prepared. Supports and NiMo catalysts were characterized by nitrogen physisorption, XRD, ammonia TPD, temperature programmed reduction (TPR), UV–vis DRS and scanning electron microscopy (SEM–EDX). It was found that Ni and Mo oxide species were well dispersed in all Ti-containing catalysts. However, TPR characterization showed that there were some differences in the characteristics of Mo oxide species supported on Ti-SBA materials and nanotubular titania supports. The above was attributed mainly to the differences in the supports' chemical composition leading to some differences in their acidity and the metal–support interactions. HRTEM characterization of sulfided NiMo catalysts also showed that the morphology of the MoS₂

particles was different on the Ti-SBA supports and on titania nanotubes. In the first case, MoS₂ crystallites were 3–4 nm in length and formed by 2 layers. On the NT supports, MoS₂ particles of similar length were observed, but formed principally by just 1 layer. In both cases, the fraction of Mo atoms located on the edge surface of MoS₂ crystallites was the same ($f_{\text{Mo}} \sim 0.3$). All NiMo catalysts prepared using Ti-containing supports of different types showed high catalytic activity for the simultaneous HDS of both DBT and 4,6-DMDBT molecules. In the HDS of 4,6-DMDBT, their activities were about twice higher than that of the NiMo/ γ -Al₂O₃ reference. Regarding selectivity, for DBT HDS, the presence of titania in the supports resulted in an increase in the proportion of CHB product, whereas for 4,6-DMDBT, a different behavior was observed. NiMo catalysts supported on Ti-SBA-15 and Ti-SBA-16 showed similar selectivity as the NiMo/ γ -Al₂O₃. These three catalysts desulfurized 4,6-DMDBT principally through the HYD pathway of the reaction. On the contrary, the catalysts supported on titania nanotubes allowed reaching high conversions of 4,6-DMDBT with a much lower ratio of MCHT/DMBP products. This indicates that these catalysts were able to desulfurize 4,6-DMDBT not only through the HYD route, but also via the DDS pathway. This is an interesting result which we relate to high dispersion of the MoS₂ active phase and the particular morphology of the nanotubular titania support.

Acknowledgments

Financial support by Consejo Nacional de Ciencia y Tecnología (CONACYT, México) (Project 220175 and Ph.D. scholarship to J.C.M.-O.) and DGAPA-UNAM (PAPIIT project IN-113715) is gratefully acknowledged. The authors thank I. Puente Lee, C. Salcedo Luna, M. Aguilar Franco and A. Morales Espino, for technical assistance with electron microscopy (HRTEM, SEM–EDX), powder and small-angle XRD characterizations.

References

- [1] S. Eijsbouts, A.A. Battiston, G.C. Van Leerdam, *Catal. Today* 130 (2008) 361.
- [2] T.C. Ho, *Catal. Today* 98 (2004) 3.
- [3] V. Chandra Srivastava, *RSC Adv.* 2 (2012) 759.
- [4] A. Stanislaus, A. Marafi, M.S. Rana, *Catal. Today* 153 (2010) 1.
- [5] I.V. Babich, J.A. Moulijn, *Fuel* 82 (2003) 607.
- [6] F.L. Plantenga, R.G. Leliveld, *Appl. Catal. A: Gen.* 248 (2003) 1.
- [7] S. Eijsbouts, F. Plantenga, B. Leliveld, Y. Inoue, K. Fujita, *Am. Chem. Soc. Div. Fuel Chem. Prepr.* 48 (2003) 494.
- [8] M.C. Kerby, T.F. Degnan Jr., D.O. Marler, J.S. Beck, *Catal. Today* 104 (2005) 55.
- [9] R. Huirache-Acuña, M.A. Albiter, J. Espino, C. Ornelas, G. Alonso-Núñez, F. Paraguay-Delgado, J.L. Rico, R. Martínez-Sánchez, *Appl. Catal. A: Gen.* 304 (2006) 124.
- [10] A. Olivas, D.H. Galván, G. Alonso, S. Fuentes, *Appl. Catal. A: Gen.* 352 (2009) 10.
- [11] Y. Yi, B. Zhang, X. Jin, L. Wang, C.T. Williams, G. Xiong, D. Su, C. Liang, *J. Mol. Catal. A: Chem.* 351 (2011) 120.
- [12] Y. Gochi, C. Ornelas, F. Paraguay, S. Fuentes, L. Alvarez, J.L. Rico, G. Alonso-Núñez, *Catal. Today* 107–108 (2005) 531.
- [13] H. Shimada, *Catal. Today* 86 (2003) 17.
- [14] S. Yoshinaka, K. Segawa, *Catal. Today* 45 (1998) 293.
- [15] J.C. Amezcua, L. Lizama, C. Salcedo, I. Puente, J.M. Domínguez, T. Klimova, *Catal. Today* 107–108 (2005) 578.
- [16] O.Y. Gutiérrez, G.A. Fuentes, C. Salcedo, T. Klimova, *Catal. Today* 116 (2006) 485.
- [17] J. Escobar, J.A. Toledo, M.A. Cortés, M.L. Mosqueira, V. Pérez, G. Ferrat, E. López-Salinas, E. Torres-García, *Catal. Today* 106 (2005) 222.
- [18] M.A. Cortés-Jácome, J. Escobar, C. Angeles Chávez, E. López-Salinas, E. Romero, G. Ferrat, J.A. Toledo-Antonio, *Catal. Today* 130 (2008) 56.
- [19] J.A. Toledo-Antonio, M.A. Cortés-Jácome, C. Angeles-Chávez, J. Escobar, M.C. Barrera, E. López-Salinas, *Appl. Catal. B: Environ.* 90 (2009) 213.
- [20] C. Guo, Y. Wu, X. Wang, B. Yang, *J. Energy Chem.* 22 (2013) 517.
- [21] R. Palcheva, L. Dimitrov, G. Tyuliev, A. Spojakina, K. Jiratova, *Appl. Surf. Sci.* 265 (2013) 309.
- [22] D. Zhao, Q. Huo, J. Feng, B.F. Chmelka, G.D. Stucky, *J. Am. Chem. Soc.* 120 (1998) 6024.
- [23] D. Zhao, J. Feng, Q. Huo, N. Melosh, G.H. Fredrickson, B.F. Chmelka, G.D. Stucky, *Science* 279 (1998) 548.
- [24] T. Yamada, H. Zhou, K. Asai, I. Honma, *Mater. Lett.* 56 (2002) 93.

- [25] P. Van Der Voort, M. Benjelloun, E.F. Vansant, *J. Phys. Chem. B* 106 (2002) 9027.
- [26] T. Kasuga, M. Hiramatsu, A. Hoson, T. Sekino, K. Nijjara, *Adv. Mater.* 11 (1999) 1307.
- [27] E. Morgado Jr., M.A.S. de Abreu, G.T. Moure, B.A. Marinkovic, P.M. Jardim, A.S. Araujo, *Chem. Mater.* 19 (2007) 665.
- [28] G. Leofanti, M. Padovan, G. Tozzola, B. Venturelli, *Catal. Today* 41 (1998) 207.
- [29] Q. Chen, G.H. Du, S. Zhang, L.-M. Peng, *Acta Crystallogr. B* 58 (2002) 587.
- [30] E. Morgado Jr., M.A.S. de Abreu, O.R.C. Pravia, B.A. Marinkovic, P.M. Jardim, F.C. Rizzo, A.S. Araújo, *Solid State Sci.* 8 (2006) 888.
- [31] X. Gao, I.E. Wachs, *Catal. Today* 51 (1999) 233.
- [32] J.A. Toledo-Antonio, M.A. Cortés-Jacome, S.L. Orozco-Cerros, E. Montiel-Palacios, R. Suarez-Parra, C. Angeles-Chávez, J. Navarete, E. López-Salinas, *Appl. Catal. B: Environ.* 100 (2010) 47.
- [33] Z. Luan, E.M. Maes, P.A.W. van der Heide, D. Zhao, R.S. Czernuszewicz, L. Kevan, *Chem. Mater.* 11 (1999) 3680.
- [34] R. López Cordero, A. López Agudo, *Appl. Catal. A: Gen.* 202 (2000) 23.
- [35] R. López Cordero, F.J. Gil Llambias, A. López Agudo, *Appl. Catal.* 74 (1991) 125.
- [36] J.L. Brito, J. Laine, *J. Catal.* 139 (1993) 540.
- [37] A. Sampieri, S. Pronier, S. Brunet, X. Carrier, C. Louis, J. Blanchard, K. Fajerweg, M. Breyse, *Microporous Mesoporous Mater.* 130 (2010) 130.
- [38] S. Kasztelan, H. Toulhoat, J. Grimblot, J. Bonnelle, *Appl. Catal.* 13 (1984) 127.
- [39] O.Y. Gutiérrez, T. Klimova, *J. Catal.* 281 (2011) 50.
- [40] E.J.M. Hensen, P.J. Kooyma, Y. Van der Meer, A.M. van der Kraan, V.H.J. de Beer, J.A.R. van Veen, R.A. van Santen, *J. Catal.* 199 (2001) 224.
- [41] B.C. Gates, H. Topsøe, *Polyhedron* 16 (1997) 3213.
- [42] C. Song, *Catal. Today* 86 (2003) 211.
- [43] C. Song, X. Ma, *Appl. Catal. B: Environ.* 41 (2003) 207.
- [44] C. Pophal, F. Kameda, K. Hoshino, S. Yoshinaka, K. Segawa, *Catal. Today* 39 (1997) 21.
- [45] F. Bataille, J.L. Lemberton, P. Michaud, G. Pérot, M. Vrinat, M. Lemaire, E. Schulz, M. Breyse, S. Kasztelan, *J. Catal.* 191 (2000) 409.
- [46] R.A. Ortega-Domínguez, J.A. Mendoza-Nieto, P. Hernández-Hipólito, F. Garrido-Sánchez, J. Escobar-Aguilar, S.A.I. Barri, D. Chadwick, T.E. Klimova, *J. Catal.* 329 (2015) 457.
- [47] J.N. Díaz de León, T.A. Zepeda, G. Alonso-Nuñez, D.H. Galván, B. Pawelec, S. Fuentes, *J. Catal.* 321 (2015) 51.